Effect of atomic-scale defects on the low-energy electronic structure of graphene: Perturbation theory and local-density-functional calculations

Joongoo Kang, Junhyeok Bang, Byungki Ryu, and K. J. Chang
Department of Physics, Korea Advanced Institute of Science and Technology, Daejeon 305-701, Korea
(Received 12 November 2007; published 28 March 2008)

Based on perturbation theory and local-density-functional calculations, we study the effect of atomic-scale defects, whose potentials vary on the scale of interatomic distance, on the electronic structure of graphene in the region of low energies. If defects are identical, for example, vacancies at the same sublattice sites or the Stone-Wales defects with the same orientations, the degeneracy at the Dirac point of graphene is removed with an energy splitting proportional to λ for low disorder densities (λ), which is attributed to the breaking of the intrinsic symmetry of the honeycomb lattice by the presence of atomic-scale defects. However, the degeneracy at the Dirac point is nearly restored if physically equivalent disorders, which are generated by the symmetry operations of graphene, such as reflection and rotation, coexist with similar concentrations.

DOI: 10.1103/PhysRevB.77.115453 PACS number(s): 73.22.−f, 71.55.−i, 71.23.−k, 81.05.Uw

I. INTRODUCTION

Graphene,[1] a single layer of carbon atoms packed in a honeycomb lattice, has attracted much attention because it is a two-dimensional zero-gap system, where quasiparticles are described by the Dirac-like Hamiltonian and behave like massless Dirac fermions. The Dirac fermion nature in graphene was experimentally verified by the observation of the unconventional half-integer quantum Hall effect.[2,3] Due to higher structural integrity and longer phase coherence lengths of carriers, as compared to Si-based microelectronics, graphene has high potential for applications to nanoscale electronic devices.[4] Recently, chemical sensing of an individual gas molecule was demonstrated by using chemical doping effect in graphene.[5]

For practical applications of graphene to nanoelectronics, it is important to understand the effect of disorders on the electronic structure because the transport properties rely on the electronic structure. Despite the fact that graphene is a strictly two-dimensional material, recent experiments showed that suspended graphene sheets exhibit intrinsic microscopic roughening.[6] At a finite temperature, the presence of structural defects such as edges and dislocations is unavoidable.[7] In addition, the electronic structure of graphene can be modified by ionized impurities in substrate and interactions between graphene and substrate atoms. In the presence of long-range disorders, with slowly varying potentials on the scale of the interatomic distance, it was shown for metallic carbon nanotubes[8,9] and graphene[10] that the pseudospin which is made of two equivalent carbon sublattices is conserved, leading to the perfect transmission of electron. On the other hand, atomic-scale defects, with the potential range of the lattice constant of graphene, can induce pseudo-spin-flip scattering.[8–10] There have been several theoretical attempts to investigate the effect of the Coulomb scatterers on the quantum transport of the Dirac fermions.[11,12] The electronic properties of impurities and carbon vacancies at the graphene lattice sites have also been studied.[7,13–15] Nevertheless, the general characteristics of disorder potentials for arbitrary atomic-scale defects and their effect on the electronic structure of graphene are still not fully understood yet.

In this work, we use a combined approach of perturbation theory and local-density-functional calculations to investigate the low-energy electronic structure near the Dirac point of graphene in the presence of atomic-scale defects. For various atomic-scale defects, such as carbon vacancies, displaced carbon atom, and the Stone-Wales defects, we study the characteristics of disorder potentials using symmetry arguments and analyze the effect of disorders on the energy splitting at the Dirac point. In the regime of low defect densities, we find from the perturbation approach that if defects are identical, the energy spitting is generally proportional to the defect density, regardless of the type of defects. When physically equivalent defects, which form a complete disorder set, are introduced into graphene with similar concentrations, we find that the degeneracy at the Dirac point and the linear band dispersion are nearly recovered. We confirm the results of the perturbation approach by performing local-density-functional calculations. We also discuss the electronic structure of localized defect states.

The paper is organized as follows. In Sec. II, general graphene states near the Dirac point are given. In Sec. III, intravalley and intervalley scatterings by an atomic-scale defect are discussed for electrons with low energies near the Dirac point. In Sec. IV, the characteristics of disorder potentials for various atomic-scale defects are described based on the symmetry arguments. In Sec. V, the perturbation approach is used to see the effect of atomic-scale defects on the low-energy electronic structure of graphene. In Sec. VI, the method and detailed results of first-principles calculations are given for the electronic structure of graphene in the presence of carbon vacancies, displaced carbon atoms, and the Stone-Wales defects. Finally, in Sec. VII, the results of the perturbation theory and first-principles calculations are compared and discussed for the energy splitting, the gap closeness, and the formation of localized defect states.

II. GRAPHENE STATES NEAR THE DIRAC POINT

The low-energy band structure of graphene near two inequivalent Brillouin zone corners, K and $\bar{K}$ [Fig. 1(a)], can

 ©2008 The American Physical Society

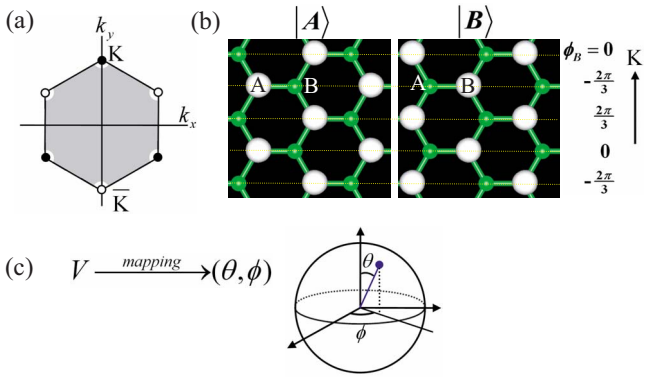

FIG. 1. (Color online) (a) The Brillouin zone of graphene and (b) the charge densities obtained from the GGA calculations for the perfect graphene states, $|A\rangle$ and $|B\rangle$, are drawn. (c) The disorder potential can be mapped onto a (θ,ϕ) point on a unit sphere.

be described by cones with linear dispersion. At the Dirac point, electron and hole states are composed of two states, $|A\rangle$ and $|B\rangle$, which are exclusively located on the sublattices, A and B, respectively, with the Bloch phase ϕ_B of the K (or $\bar{K}$) point [Fig. 1(b)]. Due to the degeneracy, general eigenstates at the Dirac point are given in the following form

$$|\theta,\phi\rangle_1 = \cos\frac{\theta}{2}|A\rangle + e^{i\phi}\sin\frac{\theta}{2}|B\rangle,$$

$$|\theta,\phi\rangle_2 = \sin\frac{\theta}{2}|A\rangle - e^{i\phi}\cos\frac{\theta}{2}|B\rangle, \tag{1}$$

where θ determines the relative amplitudes on the two sublattices and ϕ is the phase difference between the $|A\rangle$ and $|B\rangle$ states. Then, these states are geometrically represented by a point on the unit sphere [Fig. 1(c)]. In the vicinity of the Dirac point, electron (+) and hole (−) states, which have the energy dispersions, $E_{\mathbf{k}}=\hbar v|k|$ and $-\hbar v|k|$, respectively, are described by

$$\langle \mathbf{r}|\mathbf{k}(K)\rangle_{\pm} = \frac{e^{i\mathbf{k}\cdot\mathbf{r}}}{\sqrt{2}}[\psi_{A,K}(\mathbf{r}) \pm e^{i\phi(\mathbf{k})}\psi_{B,K}(\mathbf{r})], \tag{2}$$

where $\phi(\mathbf{k})=\tan^{-1}(k_y/k_x)$, $\mathbf{k}$ is the wave vector measured with respect to the K point, and the Bloch functions, $\psi_{A,K}$ and $\psi_{B,K}$, at the K point are defined as $\psi_{A,K}(\mathbf{r})=\langle \mathbf{r}|A\rangle$ and $\psi_{B,K}(\mathbf{r})=\langle \mathbf{r}|B\rangle$. It is convenient to regard the sublattice degrees of freedom as a pseudopsin, choosing the $|A\rangle$ and $|B\rangle$ states as the spin-up and spin-down states, respectively. In this two-component formalism, the graphene states in Eq. (2) are represented by

$$\Psi_{\mathbf{k}(K),\pm}(\mathbf{r}) = \frac{e^{i\mathbf{k}\cdot\mathbf{r}}}{\sqrt{2}}\begin{bmatrix} 1 \\ \pm e^{i\phi(\mathbf{k})} \end{bmatrix}. \tag{3}$$

If both the K and $\bar{K}$ points are simultaneously considered, the spinor has four components, like the spinor that describes electrons and positrons in the Dirac equation.

III. INTRAVALLEY AND INTERVALLEY SCATTERINGS

If an atomic-scale defect D is introduced into graphene with a sample size of L, it gives rise to a disorder potential V_D, which varies on the scale of interatomic distance. First, we examine an intravalley scattering by the disorder potential V_D which is formed around the atomic-scale defect D located at $\mathbf{r_D}$. Here, $\mathbf{r_D}$ represents the position of the defect D, which belongs to the unit cell specified by $m\mathbf{a}_1+n\mathbf{a}_2$, where $\mathbf{a}_1$ and $\mathbf{a}_2$ are the primitive lattice vectors of graphene and m and n are integers. Let us consider electrons with large wavelengths, i.e., $\mathbf{k}\simeq 0$ in the vicinity of the Dirac point K. Using the graphene states in Eq. (2), we write the matrix elements for the intravalley scattering such as

$$\langle \mathbf{k}(K)|V_D|\mathbf{k}'(K)\rangle = \langle \mathbf{k}(K)|V_D(\mathbf{r}-\mathbf{r_D})|\mathbf{k}'(K)\rangle. \tag{4}$$

The scattering process occurs for small wave vectors, i.e., $\mathbf{k}(\mathbf{k}')\simeq 0$, and the disorder potential $V_D(\mathbf{r})$ is atomic ranged around $\mathbf{r}=0$. We change the variable $\mathbf{r}-\mathbf{r_D}$ by $\mathbf{r}$ and approximate the phase term by $e^{i(\mathbf{k}'-\mathbf{k})\cdot\mathbf{r}}\simeq 1$. Then, the scattering amplitude in terms of the pseudospin states in Eq. (3) becomes

$$\langle \mathbf{k}(K)|V_D|\mathbf{k}'(K)\rangle \simeq \left\langle \Psi_{\mathbf{k}(K)}\left|\frac{\delta(\mathbf{r}-\mathbf{r_D})}{N_c}V_{KK}\right|\Psi_{\mathbf{k}'(K)}\right\rangle, \tag{5}$$

where V_{KK} is defined as

$$V_{KK} = N_c\begin{bmatrix} \langle\psi_{A,K}|V_D(\mathbf{r})|\psi_{A,K}\rangle & \langle\psi_{A,K}|V_D(\mathbf{r})|\psi_{B,K}\rangle \\ \langle\psi_{B,K}|V_D(\mathbf{r})\psi_{A,K}\rangle & \langle\psi_{B,K}|V_D(\mathbf{r})|\psi_{B,K}\rangle \end{bmatrix}, \tag{6}$$

and N_c is the total number of carbon atoms in the sample, i.e., twice the number of the A or B sublattice sites.

In the case of intervalley scattering, the two Dirac points, K and $\bar{K}$, are involved. Using the Bloch functions at the K and $\bar{K}$ points, which are related by $\psi_{j,\bar{K}}=e^{-i(\mathbf{K}-\bar{\mathbf{K}})\cdot\mathbf{r}}\psi_{j,K}$, with $j=A$ or B, we can write the intervalley scattering amplitude such as

$$\langle \mathbf{k}(K)|V_D|\mathbf{k}'(\bar{K})\rangle = \langle \mathbf{k}(K)|V_D(\mathbf{r}-\mathbf{r_D})|\mathbf{k}'(\bar{K})\rangle. \tag{7}$$

With the coordinate change and the approximation of $e^{i(\mathbf{k}'-\mathbf{k})\cdot\mathbf{r}}\simeq 1$, Eq. (7) is similarly rewritten as

$$\langle \mathbf{k}(K)|V_D|\mathbf{k}'(\bar{K})\rangle \simeq \left\langle \Psi_{\mathbf{k}(K)}\left|\frac{\delta(\mathbf{r}-\mathbf{r_D})}{N_c}e^{-i(\mathbf{K}-\bar{\mathbf{K}})\cdot\mathbf{r_D}}V_{K\bar{K}}\right|\Psi_{\mathbf{k}'(\bar{K})}\right\rangle, \tag{8}$$

where $V_{K\bar{K}}$ is defined as

$$V_{K\bar{K}} = N_c\begin{bmatrix} \langle\psi_{A,K}|V_D(\mathbf{r})|\psi_{A,\bar{K}}\rangle & \langle\psi_{A,K}|V_D(\mathbf{r})|\psi_{B,\bar{K}}\rangle \\ \langle\psi_{B,K}|V_D(\mathbf{r})|\psi_{A,\bar{K}}\rangle & \langle\psi_{B,K}|V_D(\mathbf{r})|\psi_{B,\bar{K}}\rangle \end{bmatrix}. \tag{9}$$

From Eqs. (5) and (8), the disorder potential V_D in the vicinity of the Dirac points, K and $\bar{K}$, is finally written in a 4×4 matrix form, which satisfies the properties of Hermicity and time-reversal symmetry,

TABLE I. Classification of atomic-scale defects into four groups by the broken symmetries of the honeycomb lattice induced by a disorder D. The disorder potential of D is mapped onto a (θ,ϕ) point on the unit sphere in Fig. 1(c). For each defect group, defect elements, which form a complete disorder set, $\{D\}^*$, are listed. The reflection symmetry between the two sublattices is preserved if there exists a line bisecting two adjacent A and B sites such that a mirror image of D with respect to this line is transformed back into D by the lattice vectors of graphene. Similarly, if a defect D preserves the threefold rotational symmetry, configurations obtained by rotating D by $\pm 120°$ with respect to an arbitrary lattice site are transformed back into D by the lattice vectors of graphene.

Group	Reflection symmetry	Threefold symmetry	(θ,ϕ)	$\{D\}^*$
I	Preserved	Preserved	Undetermined	$\{D\}$
II	Broken	Preserved	$\theta=0,\pi$	$\{D,\tilde{D}\}$
III	Preserved	Broken	$(\theta,\phi)=(\frac{\pi}{2},\frac{n\pi}{3})$, $n=$integer	$\{D,D_{\mathrm{rot}}^{120°},D_{\mathrm{rot}}^{-120°}\}$
IV	Broken	Broken	$\theta\neq 0,\pi$ $(\theta,\phi)\neq(\frac{\pi}{2},\frac{n\pi}{3})$, $n=$integer	$\{D,\tilde{D},D_{\mathrm{rot}}^{\pm 120°},\tilde{D}_{\mathrm{rot}}^{\pm 120°}\}$

$$V_D=\frac{\delta(\mathbf{r}-\mathbf{r}_D)}{N_c}\begin{bmatrix} V_{KK} & e^{-i(\mathbf{K}-\bar{\mathbf{K}})\cdot\mathbf{r}_D}V_{K\bar{K}} \\ e^{i(\mathbf{K}-\bar{\mathbf{K}})\cdot\mathbf{r}_D}V_{K\bar{K}}^{\dagger} & V_{\bar{K}\bar{K}} \end{bmatrix}, \quad (10)$$

where V_{KK} $(=V_{\bar{K}\bar{K}})$ and $V_{K\bar{K}}$ are given by 2×2 submatrices and associated with intravalley and intervalley scatterings, respectively. Here, we point out that both V_{KK} and $V_{K\bar{K}}$ do not depend on the position $(\mathbf{r_D})$ of the defect and the sample size L. We note that since the disorder potential is atomic ranged, it can be given by a δ function for carriers with sufficiently small wave vectors.[13,14]

Let the eigenstates of V_{KK} be $|\theta,\phi\rangle_1$ and $|\theta,\phi\rangle_2$ [Eq. (1)], with the eigenvalues of ε_1 and ε_2, respectively. If $\varepsilon_1\neq\varepsilon_2$ $(>\varepsilon_1)$, the corresponding (θ,ϕ) values are well defined. Then, similar to the eigenstates, a given disorder potential can be mapped onto a point (θ,ϕ) on the unit sphere in Fig. 1(c). If the basis vectors, $|A\rangle$ and $|B\rangle$, are used, the Hermitian matrix V_{KK} in Eq. (10) is transformed into the following form

$$V_{KK}(D)=\begin{bmatrix} \varepsilon_1\cos^2\frac{\theta}{2}+\varepsilon_2\sin^2\frac{\theta}{2} & \frac{\varepsilon_1-\varepsilon_2}{2}e^{-i\phi}\sin\theta \\ \frac{\varepsilon_1-\varepsilon_2}{2}e^{i\phi}\sin\theta & \varepsilon_1\sin^2\frac{\theta}{2}+\varepsilon_2\cos^2\frac{\theta}{2} \end{bmatrix}. \quad (11)$$

IV. ATOMIC-SCALE DEFECTS AND SYMMETRIES

For a given atomic-scale defect D, we expect that other defects, $\tilde{D}$ and $D_{\mathrm{rot}}^{\pm 120°}$, also exist due to the symmetry of the graphene lattice, where $\tilde{D}$ is a mirror image of D with respect to the line bisecting two adjacent A and B sites and $D_{\mathrm{rot}}^{\pm 120°}$ denote configurations obtained by rotating D by $\pm 120°$ with respect to an arbitrary A or B site. These defects are physically equivalent to the defect D and likely to be formed with the same proportions as that of D. In general, a defect D' is *physically equivalent* to the defect D if D' is generated by applying the symmetry operations of graphene on D. Using symmetry arguments at the K point, we easily obtain from $V_{KK}(D)$ in Eq. (11) the potential matrices for $\tilde{D}$ and $D_{\mathrm{rot}}^{\pm 120°}$,

$$V_{KK}(\tilde{D})=V_{KK}(D)\big|_{(\theta,\phi)\to(\pi-\theta,-\phi)},$$

$$V_{KK}(D_{\mathrm{rot}}^{\pm 120°})=V_{KK}(D)\big|_{(\theta,\phi)\to(\theta,\phi\mp 2\pi/3)}. \quad (12)$$

Then, the eigenstates of $V_K(\tilde{D})$ and $V_K(D_{\mathrm{rot}}^{\pm 120°})$ are given by $|\theta,\phi\rangle_{1,2}^{\mathrm{mirror}}=|\pi-\theta,-\phi\rangle_{1,2}$ and $|\theta,\phi\rangle_{1,2}^{\pm 120°}=|\theta,\phi\mp\frac{2\pi}{3}\rangle_{1,2}$, respectively.

The linear band structure of graphene with the electron-hole degeneracy at the K and $\bar{K}$ points is attributed to the symmetries of the honeycomb lattice: (i) the reflection symmetry between two sublattice sites and (ii) the threefold rotational symmetry around an arbitrary lattice site. These symmetries can be broken by introducing an atomic-scale defect into graphene. Depending on the type of broken symmetries, atomic-scale defects can be classified into four groups, as shown in Table I. In each group, physically equivalent defects form a complete disorder set $\{D\}^*$.

It was shown that alkali metal atoms doped in graphene energetically favor the top sites of hexagon centers.[16,17] Since these adatom defects do not break the reflection and threefold rotational symmetries, they belong to group I (Table I). If an ideal carbon vacancy, which is just a missing atom with no significant reconstruction surrounding it, is created at a A sublattice site (Fig. 2), the reflection symmetry between the two sublattices is broken, while the threefold symmetry is preserved. Thus, ideal carbon vacancies are classified as group-II defects. Actually, several studies[18,19] showed that the ideal vacancy is energetically unstable with respect to a reconstructed structure in which two dangling bonds are eliminated by rebonding and one atom is significantly displaced out of the plane. This reconstructed vacancy structure not only breaks the reflection and threefold rotational symmetries of the ideal vacancy but also the planar symmetry of the graphene layer, being considered as group-IV defect. Since the reconstructed structure is accom-

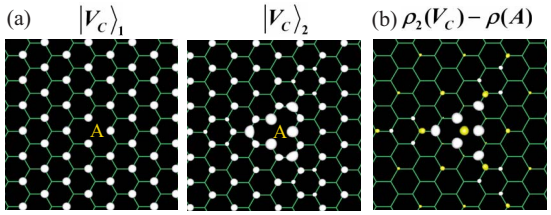

FIG. 2. (Color online) In the presence of an ideal C vacancy at the *A* sublattice site, (a) the charge densities obtained from the GGA calculations for the defect states at the *K* point, $|V_C\rangle_1$ and $|V_C\rangle_2$, and (b) the difference of the charge densities for $|V_C\rangle_2$ and $|A\rangle$ are drawn.

panied with large atomic relaxations which induce strong perturbations for the graphene states near the Dirac point, the perturbation approach may not be appropriate. Here, we focus on ideal vacancies throughout this work. If a single carbon atom is displaced along the z direction perpendicular to the graphene sheet (henceforth, denoted as a δz defect), only the reflection symmetry between the sublattices is broken, similar to the ideal C vacancy. On the other hand, a Stone-Wales (SW) defect [Fig. 3(a)], which consists of five- and seven-membered rings, maintains the reflection symmetry between the sublattices, whereas it breaks the threefold symmetry around the defect site. Thus, this topological defect belongs to group III.

The symmetries of the defect D impose constraints on the (θ,ϕ) values of the potential matrix in Eq. (11). If a defect D belongs to group I, since $\tilde{D}$ and $D_{\mathrm{rot}}^{\pm 120^\circ}$ are identical to D, it requires $\varepsilon_1=\varepsilon_2$. In this case, the (θ,ϕ) values are not determined, and the disorder potential does not affect the sublattice degrees of freedom in graphene. For group-II defects, since the threefold rotational symmetry is preserved by rotations of $\pm 120^\circ$, the allowed values for θ are 0 and π. Although ϕ is undetermined, it has no physical meaning for $\theta=0$ or π. In a similar manner, we find that the disorder potential $V_{KK}(D)$ of a group-III defect is mapped onto one of

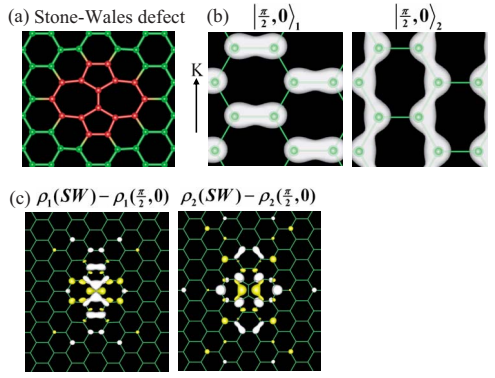

FIG. 3. (Color online) (a) The atomic structure of a Stone-Wales defect and (b) the charge densities (white clouds) for the zeroth-order states, $|\frac{\pi}{2},0\rangle_{1,2}$, at the *K* point are drawn. (c) The differences of the charge densities obtained from the GGA calculations for $|\mathrm{SW}\rangle_{1,2}$ and $|\frac{\pi}{2},0\rangle_{1,2}$, are given, where $|\mathrm{SW}\rangle_{1,2}$ denote the defect states in the presence of a single SW defect.

six points, $(\frac{\pi}{2},\frac{n\pi}{3})$ with n integer, on the unit sphere in Fig. 1(c). For group-IV defects, all (θ,ϕ) values are available except for those constrained for group-II and group-III defects.

V. PERTURBATION THEORY FOR ENERGY SPLITTING

A. Identical defects

Due to the pseudospin and valley degeneracies, a disorder potential was shown to be represented by a 4×4 matrix [Eq. (10)]. The matrix elements for the intervalley scattering contain the position-dependent term, $e^{-i(\mathbf{K}-\bar{\mathbf{K}})\cdot(m\mathbf{a}_1+n\mathbf{a}_2)}$, where m and n denote the positions of disorders. If a sufficiently large amount of disorders are randomly distributed, the phase factors from different disorder positions are averaged out by the relation $\Sigma_{m,n}e^{-i(\mathbf{K}-\bar{\mathbf{K}})\cdot(m\mathbf{a}_1+n\mathbf{a}_2)}\rightarrow 0$. Since the intervalley scattering is suppressed upon the disorder ensemble average, disorders can be treated only by using the 2×2 intravalley scattering matrices, V_{KK} and $V_{\overline{KK}}$ in Eq. (10). If we consider the scattering process from $\mathbf{k}=0$ to $\mathbf{k}'=0$, the scattering matrix V_{KK}/N_c just represents the first-order perturbation by a single defect to the energy at the Dirac point in the degenerate perturbation theory. As discussed earlier, both V_{KK} and $V_{\overline{KK}}$ are independent of the disorder position. Thus, if graphene contains identical atomic-scale defects, with the defect concentration of λ, the effect of disorders at the *K* point can be described by the total disorder potential, $V=\lambda V_{KK}$, within the first-order perturbation theory. Here, the dimensionless density λ is defined as the ratio of the number of defects (N_D) to the total number of carbon atoms in graphene, i.e., $\lambda=N_D/N_c$. The perturbation theory can be properly used in the dilute limit of λ, where interactions between disorders are neglected.

Since the eigenvalues of V_{KK} are ε_1 and ε_2 [Eq. (11)], the effect of identical disorders is to break up the electron-hole degeneracy at the Dirac point. The first-order energy splitting at the Dirac point is proportional to the defect density,

$$\Delta_1=\lambda(\varepsilon_2-\varepsilon_1). \tag{13}$$

Then, the zeroth-order eigenstates are given by the extended states, $|\theta,\phi\rangle_1$ and $|\theta,\phi\rangle_2$ in Eq. (1), while higher-order corrections of λ reflect defect-associated localized states at low energies near the Dirac point. In the region far from defects, the $|\theta,\phi\rangle_{1,2}$ states exhibit charge-ordered patterns determined by the (θ,ϕ) values, with the same periodicity as the graphene lattice.

B. Physically equivalent defects

The cancellation of intervalley scatterings also occurs for physically equivalent defects which form a complete disorder set $\{D\}^*$ (Table I), if the amount of randomly distributed disorders is sufficiently large for each element. Then, the effect of physically equivalent defects is also described by the intravalley scattering matrix, which gives by the first-order disorder potential proportional to the identity matrix (I). In group II, to which C vacancy and δz defects belong, the complete disorder set consists of two elements, D and $\tilde{D}$.

If the total defect density of D and $\tilde{D}$ is λ, the total disorder potential is reduced to $\lambda(\varepsilon_1+\varepsilon_2)I/2$ to the first order of λ, giving an overall band shift by $\lambda(\varepsilon_1+\varepsilon_2)/2$ at the Dirac point. For the SW defects belonging to group III, three elements, D, $D_{\text{rot}}^{120°}$, and $D_{\text{rot}}^{-120°}$, form the complete disorder set. In this case, the total disorder potential matrix has only the diagonal elements, $\lambda(\varepsilon_1 \cos^2\frac{\theta}{2}+\varepsilon_2 \sin^2\frac{\theta}{2})$ and $\lambda(\varepsilon_1 \sin^2\frac{\theta}{2}+\varepsilon_2 \cos^2\frac{\theta}{2})$, for the total defect density of λ. Since $\theta=\frac{\pi}{2}$ for the SW defects, the disorder potential causes a constant shift of the band by $\lambda(\varepsilon_1+\varepsilon_2)/2$.

For an arbitrary disorder D, if a complete disorder set[20] is given by

$$\{D\}^* = \{D, D_{\text{rot}}^{120°}, D_{\text{rot}}^{-120°}, \tilde{D}, \tilde{D}_{\text{rot}}^{120°}, \tilde{D}_{\text{rot}}^{-120°}\}, \tag{14}$$

the first-order disorder potential satisfies the relation,

$$\sum_{i\in\{D\}^*} V_{KK}(i) = 3(\varepsilon_1+\varepsilon_2)I. \tag{15}$$

Since the disorder potential by defects in a complete disorder set only shifts the energies, the gap closeness occurs at the Dirac point, and the degeneracy at the Dirac point is nearly recovered to the first order of λ, regardless of the (θ,ϕ) values in Eq. (11). This result indicates that the broken symmetries of the honeycomb lattice by a specific defect D are recovered upon the ensemble average over physically equivalent defects in $\{D\}^*$. The gap-closing effect is consistent with the general property of disordered systems, where the energy spacing usually goes to zero in the thermodynamic limit.

VI. RESULTS OF LOCAL-DENSITY-FUNCTIONAL CALCULATIONS

A. Calculational method

To confirm the results of the perturbation approach for the energy splitting and the gap-closing effect by atomic-scale defects at the Dirac point, we performed first-principles calculations within the density-functional-theory framework. We used the generalized gradient approximation (GGA)[21] for the exchange-correlation potential, which is implemented in the VASP code.[22] We employed ultrasoft pseudopotentials[23] for the ionic potentials. All the wave functions were expanded in plane waves up to an energy cutoff of 287 eV. We considered various atomic-scale defects including carbon-vacancy defect, δz defect, and the Stone-Wales defect, with varying their defect concentrations. We chose several supercell geometries with different sizes and shapes such as hexagonal and tetragonal supercells. In these supercell geometries, the K and $\bar{K}$ points with twofold degeneracy are folded into two different points in the supercell Brillouin zone. Thus, intervalley scatterings are exactly canceled out, and intravalley scatterings described by 2×2 matrices were used. We took the separation of 8 Å between two adjacent graphene sheets, which ensures for prohibiting the coupling of neighboring supercells by testing distances up to 10 Å. The Brillouin zone summation of the charge densities was carried out by using a special k-point set generated by 3 $\times 3$ Monkhorst–Pack mesh for the 16×16 hexagonal supercell, where numbers by $n_1\times n_2$ denote integer multiples of the graphene lattice vectors, $\mathbf{a}_1$ and $\mathbf{a}_2$. For other supercells, we selected k-point sets which give similar numerical accuracies to that obtained for the 16×16 hexagonal supercell.

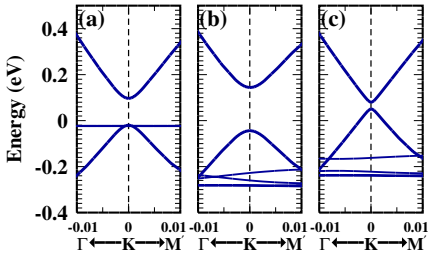

FIG. 4. (Color online) The GGA band structures are plotted in the vicinity of the K point for graphene sheets with (a) a single C vacancy, (b) two identical C vacancies at the same sublattice sites, and (c) two physically equivalent C vacancies at the different sublattice sites, which form a complete disorder set. Numbers on the symmetry lines (Γ-K and K-M') denote wave vectors (k) in unit of the wave vector at the K point. The energy of the Dirac point in perfect graphene is set to zero.

B. Carbon-vacancy and δz defects

When an ideal carbon vacancy (V_C) is introduced to an A sublattice site in the 10×10 hexagonal supercell, corresponding to $\lambda=0.005$, we find the energy splitting of $\Delta=116$ meV at the K point [Fig. 4(a)], which results from the broken symmetry between the two sublattices. The flat band near the valence band edge is caused by the dangling bond σ orbitals of V_C, which do not interact with the graphene pseudospin states. At the K point, we note that the lower-energy state $|V_C\rangle_1$ is almost identical to $|B\rangle$. On the other hand, as discussed earlier, the higher-energy state $|V_C\rangle_2$ is given by a combination of the extended state $|A\rangle$ for the region far from the V_C defect and the localized π state around the defect site [Fig. 2(b)]. Our calculations indicate that the potential of V_C at the A sublattice is mapped onto the point, $\theta=\pi$, consistent with the symmetry arguments for group II defects (Table I). If V_C is located at a B sublattice site, its disorder potential is mapped onto the point of $\theta=0$. Since the electron-hole degeneracy at the K point is removed by V_C, the wave functions are no longer singular for all $\mathbf{k}$ points including the K point.

If two ideal C vacancies ($\lambda=0.01$) are located at the same A or B sublattice sites, the energy gap increases to 187 meV [Fig. 4(b)]. However, the energy gap is reduced to 26.8 meV [Fig. 4(c)], when two C vacancies are separated at the different sublattice sites. The gap-closing effect by the presence of two physically equivalent C vacancies, $V_C(A)$ and $V_C(B)$, can be understood by the fact that the disorder potential to the first order of λ is $\lambda(\varepsilon_1+\varepsilon_2)I/2$, where I is the identity matrix, giving an overall band shift by $\lambda(\varepsilon_1+\varepsilon_2)/2$. Due to the higher-order terms of λ, the degeneracy of the Dirac point is still broken, with the small gap. When a larger 16×16 supercell is used, giving $\lambda=0.0039$, we find a very small energy gap of 8.8 meV in the presence of $V_C(A)$ and $V_C(B)$.

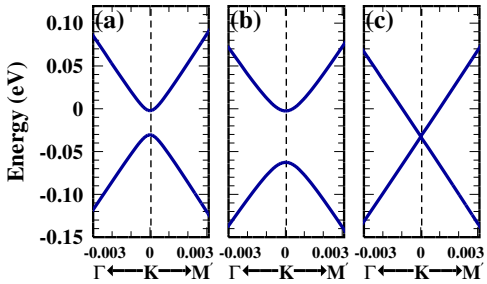

FIG. 5. (Color online) The GGA band structures are plotted in the vicinity of the K point for graphene sheets with (a) a single δz defect, (b) two identical δz defects at the same sublattice sites, and (c) two physically equivalent δz defects at the different sublattice sites, which form a complete disorder set. Numbers on the symmetry lines (Γ-K and K-M') denote wave vectors (k) in unit of the wave vector at the K point. The energy of the Dirac point in perfect graphene is set to zero.

Similarly, we find the gap-closing effect for the δz defect, which belongs to the same group (group II) as the C vacancy (Table I). With choosing the displacement of $\delta z=0.5$ Å, we calculate the energy gap at the K point to be 28.0 meV [Fig. 5(a)] for a single δz defect in the 8×8 supercell, which corresponds to $\lambda=0.0078$. When two δz defects are located at the A and B sublattice sites, the energy gap is reduced to 0.6 meV, and the energy band is shifted to lower energies by 30.3 meV [Fig. 5(c)]. On the other hand, the energy gap is found to increase by a factor of 2 in the presence of two identical δz defects [Fig. 5(b)]. We point out that although the energy splitting depends on the magnitude of δz, the general features such as the energy splitting and the gap closeness will not be affected by choosing different displacements for the δz defect.

C. Stone-Wales defect

For a single Stone-Wales defect in the 10×10 hexagonal supercell ($\lambda=0.005$), we find that the Dirac point shifts from the K point toward the M' point [Fig. 6(a)], maintaining the twofold degeneracy. Due to the band shift, the degeneracy at the K point is removed, giving the energy splitting of $\Delta=27.8$ meV. When three SW defects with the same orientation of the five- and seven-membered rings are introduced into the 10×10 supercell ($\lambda=0.015$), the movement of the Dirac point along the K-M' direction is three times larger [Fig. 6(b)]. The displacement of the Dirac point toward the M' point is nearly proportional to the density of the SW defects, consistent with previous theoretical calculations.[24] We also find that the energy splitting at the K point increases to 80.3 meV, about three times larger than that for a single SW defect. In this case, in contrast to the single SW defect, a very small gap appears at the Diract point shifted along the K-M' direction [Fig. 6(b)], which may originate from defect-defect interactions in the finite-sized supercell. If three SW defects with different orientations, D, $D_{\mathrm{rot}}^{120^\circ}$, and $D_{\mathrm{rot}}^{-120^\circ}$, are present in the 10×10 supercell, the Dirac point is almost recovered at the K point, as shown in Fig. 6(c). Since the energy gap of 6.5 meV at the K point is extremely small, the gap-closing effect also occurs by the presence of physically equivalent SW defects with different orientations.

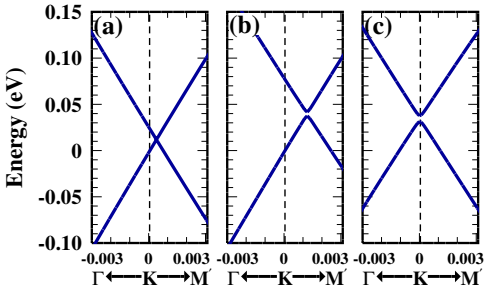

FIG. 6. (Color online) The GGA band structures are plotted in the vicinity of the K point for graphene sheets in the presence of (a) a single SW defect, (b) three identical SW defects with the same orientations, and (c) three physically equivalent SW defects with different orientations (D, $D_{\mathrm{rot}}^{120^\circ}$, $D_{\mathrm{rot}}^{-120^\circ}$), which form a complete disorder set. Numbers on the symmetry lines (Γ-K and K-M') denote wave vectors (k) in unit of the wave vector at the K point. The energy of the Dirac point in perfect graphene is set to zero.

We examined the distribution of charge densities for the two defect states, $|\mathrm{SW}\rangle_1$ and $|\mathrm{SW}\rangle_2$, which are splitted by a SW defect at the K point. In the region far from the defect site, $|\mathrm{SW}\rangle_1$ and $|\mathrm{SW}\rangle_2$ exhibit the charge-ordered patterns similar to those of the zeroth-order eigenstates, $|\frac{\pi}{2},0\rangle_1$ and $|\frac{\pi}{2},0\rangle_2$, respectively, as shown in Figs. 3(b) and 3(c). This result is consistent with the potential mapping of the SW defect onto the $(\frac{\pi}{2},0)$ point in Fig. 1(c). From the difference of the charge densities between the $|\mathrm{SW}\rangle_{1,2}$ and $|\frac{\pi}{2},0\rangle_{1,2}$ states, we note that higher-order perturbed states are localized states, with the charge densities mostly distributed around the SW defect [Fig. 3(c)].

VII. COMPARISON OF PERTURBATION THEORY AND GENERALIZED GRADIENT APPROXIMATION CALCULATIONS

A. Energy splitting

If atomic-scale defects are identical, with the defect density λ, the first-order energy splitting at the K point is proportional to λ, $\Delta_1=\lambda(\varepsilon_2-\varepsilon_1)$, according to the perturbation theory in Sec. V A. For graphene sheets with different numbers of identical defects, the GGA band structures obtained from the supercell calculations are drawn in the vicinity of the Dirac point in Figs. 4–6. When the number of identical defects increases by factors of 2 and 3 for the δz and SW defects, respectively, the energy splitting increases by the same factors, as shown in Figs. 5(b) and 6(b). For the V_{C} defect, we find that the energy splitting is enhanced by a factor of 1.6 [Fig. 4(b)], when the number of defects increases from 1 to 2 in the 10×10 supercell. A small deviation of the enhancement factor from 2 is attributed to the contributions of high-order terms of λ. Due to the use of finite-sized supercells, the defects may have an artificial periodicity. Thus, interactions between the V_{C} defects seem to be more significant, compared to the δz and SW defects.

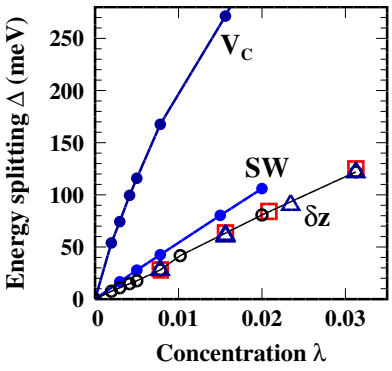

FIG. 7. (Color online) The variation of the energy splitting (Δ) calculated from the GGA at the K point is plotted as a function of the defect density λ for the C-vacancy, the Stone-Wales, and δz defects. Identical defects are used for each curve. For the δz defect, circles and squares denote the results obtained by varying the sizes of hexagonal and tetragonal supercells, respectively, whereas triangles represent those obtained by varying the number of defects for a given 8×8 supercell.

For the V_C, δz, and SW defects, Fig. 7 shows the results of our first-principles calculations for the variation of the energy splitting at the K point as a function of λ. We find that overall the energy splitting follows the linear variation with λ for low defect concentrations, in good agreement with the perturbation approach. Since ε_1 and ε_2 are determined by the disorder potential, $V_{KK}(D)$ in Eq. (11), the slope varies with the type of defect. The slopes are calculated to be 29.7, 3.9, and 5.6 eV for the C vacancy, δz (with δz=0.5 Å), and SW defects, respectively. The δz and SW defects exhibit the linear behavior even for high defect concentrations. In the case of V_C, the slope is deviated from a straight line as the defect density increases, which is caused by enhanced interactions between the defects. Here, we point out that the lines in Fig. 7 are universal in the sense that the energy splitting depends only on λ, irrelevant to the shape or size of supercells and the details of defect positions within the supercell, as long as the defects are well separated from each other. For the δz defect, we examined various concentrations using the hexagonal and tetragonal supercells with different supercell sizes and varying the number of defects for a given 8×8 supercell. We find that all the energy splittings are positioned on the same line, confirming the result of the perturbation theory that the energy splitting varies with λ.

B. Gap closeness

In Sec. V B, it was shown that physically equivalent defects in a complete disorder set $\{D\}^*$ give the first-order disorder potential proportional to the identity matrix. Since the total disorder potential only shifts the energies, the electron-hole degeneracy at the Dirac point is maintained to the first order of λ in the perturbation approach. The closeness of the energy gap will be effective if λ is sufficiently low, suppressing higher-order contributions of λ to the energy splitting. For the V_C, δz, and SW defects, the energy shift at the K point is given by $\lambda(\varepsilon_1+\varepsilon_2)/2$, if the physically equivalent defects have the same defect concentration. In this case, the Fermi point restored by physically equivalent defects at the K point will lie in the middle of ε_1 and ε_2, which are determined by identical defects with the same defect density.

In Figs. 4–6, the GGA band structures of graphene sheets with identical defects are compared to those for the sheets containing physically equivalent defects. For all the defects considered here, we find that physically equivalent defects induce the gap-closing effect, while identical defects split the energies at the K point. Although the gap-closing effect is prominent for the δz and SW defects [Figs. 5(c) and 6(c)], a small gap still remains for the V_C defect [Fig. 4(c)]. Similar to the case of identical defects, the incomplete recovery of the Dirac point is attributed to the use of the finite-sized 10×10 supercell. As mentioned in Sec. VI B, the gap closeness is more clearly seen in the larger 16×16 supercell, in which interactions between the defects are much suppressed. From the energy splitting by a single SW defect in the 10×10 supercell [Fig. 6(a)], we estimate ε_1 and ε_2 to be −0.44 and 5.12 eV, respectively, with the use of λ=0.005. The energy splitting at the K point increases by a factor of 3 when three identical SW defects are included [Fig. 6(b)]. If three physically equivalent SW defects, D, $D_{\mathrm{rot}}^{120^\circ}$, and $D_{\mathrm{rot}}^{-120^\circ}$, exist in the same supercell, the first-order perturbation theory gives the energy shift of 35 meV. This energy shift is in good agreement with the band structure obtained from first principles, which exhibits the upward shift of the Fermi level at the K point, as shown in Fig. 6(c). From Figs. 6(b) and 6(c), we confirm that the Fermi point is located at the average energy of ε_1 and ε_2. For the V_C and δz defects, we also find that the energy shifts obtained from the GGA calculations are in good agreement with the results of the perturbation approach.

In real graphene, with a sufficiently large sample size of L, physically equivalent defects in a complete disorder set may coexist with similar concentrations. Because the gap opening by one defect element in a complete disorder set is nearly compensated by other defect elements, small fluctuations in defect concentrations, which are proportional to $\sqrt{\lambda/L^2}$, can contribute to the gap opening at the K point. For C vacancies with λ=0.01, the numbers of two different vacancies, $V_C(A)$ and $V_C(B)$, which are denoted as N_A and N_B, respectively, will be around 1.9×10^5 for the sample size of 1 μm^2. When graphene has one type of the C vacancies, either $V_C(A)$ or $V_C(B)$, the induced gap is 187 meV for λ =0.01 [Fig. 4(b) or 7]. In the presence of both $V_C(A)$ and $V_C(B)$, the gap induced by a single $V_C(A)$ is nearly canceled by its mirror image $V_C(B)$. Then, the energy gap will be proportional to $|N_A-N_B|$, which is statistically an order of $\sqrt{N_A}\sim10^2$. We expect that the induced gap is only about 0.3 meV, although the concentration of V_C is in the range of 10^{13} cm^{-2}. This result indicates that in graphene with a large sample size, the energy gap at the Dirac point will be extremely small due to the gap-closing effect even in the presence of atomic-scale defects with conceivable concentrations. However, if graphene strongly interacts with substrate atoms, the graphene lattice is likely to be severely distorted, resulting in the gap opening. Recent experiments showed

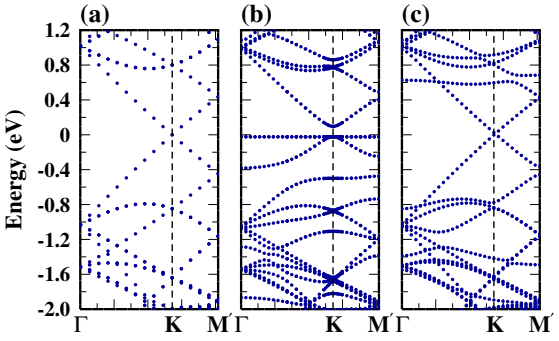

FIG. 8. (Color online) The GGA band structure of (a) perfect graphene is compared to those for graphene sheets with (b) a single C-vacancy and (c) a single SW defect in the 10×10 hexagonal supercell. The energy of the Dirac point in perfect graphene is set to zero.

that graphene epitaxially grown on SiC substrate exhibits a gap of 0.26 eV, which may be related to the broken sublattice symmetry by interactions between graphene and substrate.[25]

C. Localized defect states

Here, the perturbation approach used does not properly describe the localized defect states induced by atomic-scale defects, only giving information on the low-energy electronic structure. On the other hand, since the GGA calculations are done self-consistently by including both the σ and π orbitals of graphene, both the extended and localized states are well produced. For an ideal V_C at the A (or B) sublattice site ($\lambda=0.005$), our GGA calculations show the localized states right at the lower band edge split by the defect at the K point [Fig. 4(a)]. These localized states are associated with the dangling bond σ orbitals surrounding V_C. When two carbon vacancies are located at the same or different sublattice sites, the σ-orbital localized states are lowered by about 0.2 eV, as compared to the single vacancy [Figs. 4(b) and 4(c)]. The lowering of these localized defect states results from the fact that the Fermi level decreases in increasing the number of vacancies. Since the localized states are nearly decoupled from the graphene pseudospin states which are mainly composed of the π and π^* orbitals, they do not affect the energy splitting at the Dirac point. Other localized state associated with the π orbitals of the nearest neighboring atoms around V_C is found to lie at about 0.5 eV below the Dirac point of perfect graphene [Fig. 8(b)]. This localized state contributes to the energy splitting at the Dirac point through high-order perturbation terms. In the single π-orbital tight-binding model with the electron-hole symmetry, where only the nearest neighbor hopping energy ($t\approx2.7$ eV) is used, the localized state arisen from the π orbitals is formed at the Fermi energy, i.e., the Dirac point.[15] In this case, the gap-closing effect, which is found in our first-principles calculations, does not appear due to strong interactions between the localized state and the π and π^* orbitals at the Dirac point. If the electron-hole symmetry is broken by including the next-nearest neighbor hopping energy (t'), the localized state is shifted to lower energies from the Fermi level. We note that it requires $t'\approx0.2t$ to get the same position of the localized state as that obtained from the GGA calculations.

For a single SW defect in the 10×10 hexagonal supercell, we find three localized states at about -1.4, 0.6, and 0.9 eV with respect to the Fermi level, as shown in Fig. 8(c). Since these defect states are positioned at high energies and weakly coupled to the graphene states, as compared to the V_C defect, their effects on the electronic structure near the Dirac point are much suppressed, giving the almost linear dependence of the energy splitting on the defect density (Fig. 7).

In single-walled carbon nanotubes, recent transport measurements[26] showed that the nanotube system, in which many divacancies are randomly distributed, is within the Anderson localization regime due to the coherent backscattering of electrons by defects. In graphene, defect-induced localized states formed at low energies may also lead to the Anderson localization for large defect densities, while the Anderson localization is absent in the presence of long-range disorders.[10] If atomic-scale defects induce localized states near the Dirac point, these states may modify the low-energy electrical properties of the Dirac fermions. In recent tight-binding calculations,[27] which preserves the electron-hole symmetry, an internal localization mobility edge was shown to appear around the Fermi energy in doped graphene with vacancies, in contrast to the usual Anderson localization which exhibits a localization mobility edge at the band edges. In our first-principles calculations, since the localized states resulted from the dangling bond π orbitals of C vacancies are positioned at 0.5 eV below the Dirac point of perfect graphene, the effect of the localization mobility edge on the electron transport is only effective at high energies. In the case of SW defects, the localization mobility edge does not appear in the low energy region.

VIII. CONCLUSIONS

We have studied the effect of atomic-scale defects on the low-energy electronic structure of graphene using both the perturbation theory and the local-density-functional calculations for low defect densities. We have shown that atomic-scale defects can be classified into several groups by the type of broken symmetries by defects. If atomic-scale defects are identical, the electron-hole symmetry is generally removed, resulting in the energy splitting proportional to the defect density at the Dirac point of graphene. However, we find that the broken symmetry caused by a single defect is nearly recovered by an ensemble of physically equivalent defects, which form the complete disorder set. In graphene, since physically equivalent defects may coexist with similar proportions, the degeneracy at the Dirac point is likely to be statistically maintained to the first order of defect density.

ACKNOWLEDGMENT

This work was supported by the Korea Research Foundation under Grant No. KRF-2005-084-C00007.

[1] K. S. Novoselov, A. K. Geim, S. V. Morozov, D. Jiang, Y. Zhang, S. V. Dubonos, I. V. Grigorieva, and A. A. Firsov, Science **306**, 666 (2004).
[2] K. S. Novoselov, A. K. Geim, S. V. Morozov, D. Jiang, M. I. Katsnelson, I. V. Grigorieva, S. V. Dubonos, and A. A. Firsov, Nature (London) **438**, 197 (2005).
[3] Y. Zhang, Y.-W. Tan, H. L. Stormer, and P. Kim, Nature (London) **438**, 201 (2005).
[4] C. Berger, Z. Song, X. Li, X. Wu, N. Brown, C. Naud, D. Mayou, T. Li, J. Hass, A. N. Marchenkov, E. H. Conrad, P. N. First, and W. A. de Heer, Science **312**, 1191 (2006).
[5] F. Schedin, A. K. Geim, S. V. Morozov, E. W. Hill, P. Blake, M. I. Katsnelson, and K. S. Novoselov, Nat. Mater. **6**, 652 (2007).
[6] J. C. Meyer, A. K. Geim, M. I. Katsnelson, K. S. Novoselov, T. J. Booth, and S. Roth, Nature (London) **446**, 60 (2007).
[7] N. M. R. Peres, F. Guinea, and A. H. Castro Neto, Phys. Rev. B **73**, 125411 (2006).
[8] T. Ando and T. Nakanishi, J. Phys. Soc. Jpn. **67**, 1704 (1998).
[9] P. L. McEuen, M. Bockrath, D. H. Cobden, Y.-G. Yoon, and S. G. Louie, Phys. Rev. Lett. **83**, 5098 (1999).
[10] M. I. Katsnelson, K. S. Novoselov, and A. K. Geim, Nat. Phys. **2**, 620 (2006).
[11] K. Nomura and A. H. MacDonald, Phys. Rev. Lett. **98**, 076602 (2007).
[12] E. H. Hwang, S. Adam, and S. Das Sarma, Phys. Rev. Lett. **98**, 186806 (2007).
[13] T. Ando and K. Akimoto, J. Phys. Soc. Jpn. **73**, 1895 (2004).
[14] H. Suzuura and T. Ando, J. Phys. Soc. Jpn. **72**, 69 (2003).
[15] V. M. Pereira, F. Guinea, J. M. B. Lopes dos Santos, N. M. R. Peres, and A. H. Castro Neto, Phys. Rev. Lett. **96**, 036801 (2006).
[16] M. Khantha, N. A. Cordero, L. M. Molina, J. A. Alonso, and L. A. Girifalco, Phys. Rev. B **70**, 125422 (2004).
[17] K. Rytkönen, J. Akola, and M. Manninen, Phys. Rev. B **75**, 075401 (2007).
[18] R. H. Telling, C. P. Ewels, A. A. El-Barbary, and M. I. Heggie, Nat. Mater. **2**, 333 (2003).
[19] A. A. El-Barbary, R. H. Telling, C. P. Ewels, M. I. Heggie, and P. R. Briddon, Phys. Rev. B **68**, 144107 (2003).
[20] Besides the symmetries considered in Table I, the graphene lattice has additional symmetries such as the planar symmetry of the graphene sheet and the reflection symmetry with respect to the line passing through two arbitrary adjacent A and B sites. These symmetries can physically generate equivalent defects (D'), which do not belong to the complete set $\{D\}^*$ in Eq. (14). For each D', a complete disorder set $\{D'\}^*$ can be formed in the same way as $\{D\}^*$ is set up using the symmetry operations in Table I. Therefore, a more general complete set consists of physically equivalent defects which belong to $\{D\}^* \cup \{D'\}^*$.
[21] J. P. Perdew, in *Electronic Structure of Solids*, edited by P. Ziesche and H. Eschrig (Akademie-Verlag, Berlin, 1991).
[22] G. Kresse and J. Furthmüller, Phys. Rev. B **54**, 11169 (1996).
[23] D. Vanderbilt, Phys. Rev. B **41**, R7892 (1990).
[24] V. H. Crespi, M. L. Cohen, and A. Rubio, Phys. Rev. Lett. **79**, 2093 (1997).
[25] S. Y. Zhou, G.-H. Gweon, A. V. Fedorov, P. N. First, W. A. De Heer, D.-H. Lee, F. Guinea, A. H. Castro Neto, and A. Lanzara, Nat. Mater. **6**, 770 (2007).
[26] C. Gómez-Navarro, P. J. De Pablo, J. Gómez-Herrero, B. Biel, F. J. Garcia-Vindal, A. Rubio, and F. Flores, Nat. Mater. **4**, 534 (2005).
[27] G. G. Naumis, Phys. Rev. B **76**, 153403 (2007).